Experimental and numerical investigation of key microstructural features influencing the localization of plastic deformation in Fe-TiB2 metal matrix composite

J. Genée, Nathalie Gey, F. Bonnet, R. A. Lebensohn, Stephane Berbenni

Experimental and numerical investigation of key microstructural features influencing the localization of plastic deformation in Fe-TiB_2 metal matrix composite

J. Genée[1,2,*], N. Gey[1,2], F. Bonnet[3], R. A. Lebensohn[4], and S. Berbenni[1,2]

[1] *University of Lorraine, Arts et Métiers Paris Tech CNRS, LEM3, F-57000 Metz, France*
[2] *Laboratory of Excellence On Design of Alloy Metals for Low-mAss Structures (DAMAS), University of Lorraine, Metz, France*
[3] *ArcelorMittal Research, Voie Romaine BP30320, Maizières-les-Metz Cedex 57283, Metz, France*
[4] *Theoretical Division, Los Alamos National Laboratory, Los Alamos, NM 87845, USA*

ABSTRACT

A new generation of iron-based matrix composite reinforced by TiB_2 particles was deformed in tension to investigate at a mesoscopic scale the localization of plastic deformation in relation with characteristic microstructural features of the composite (in particular, ferrite grain boundaries and particle/matrix inter-faces). Large electron back-scattered diffraction (EBSD) maps with improved angular resolution were acquired to evaluate statistically the evolution of the geometrically necessary dislocation (GND) density from the early stage of the deformation. GNDs were found to accumulate preferentially at matrix/particle interfaces with hot-spots located at the tips of elongated particles. Additional length-scale parameters derived from EBSD data evidenced the key influence of two main microstructural features: the particle morphology and the particle clustering. Finally, we present results of an advanced full-field micromechanical model that is best suited to capture these effects, based on an enhanced crystal plasticity elasto-viscoplastic Fast Fourier Transform (EVP-FFT) formulation coupled with a phenomenological continuum Mesoscale Field Dislocation Mechanics (MFDM) theory. By taking the experimental TiB_2 particle distribution into account, the model describes qualitatively the observed effect of particle morphological features on the heterogenous distribution of GNDs.

Address correspondence to E-mail: julien.genee@univ-lorraine.fr

GRAPHICAL ABSTRACT

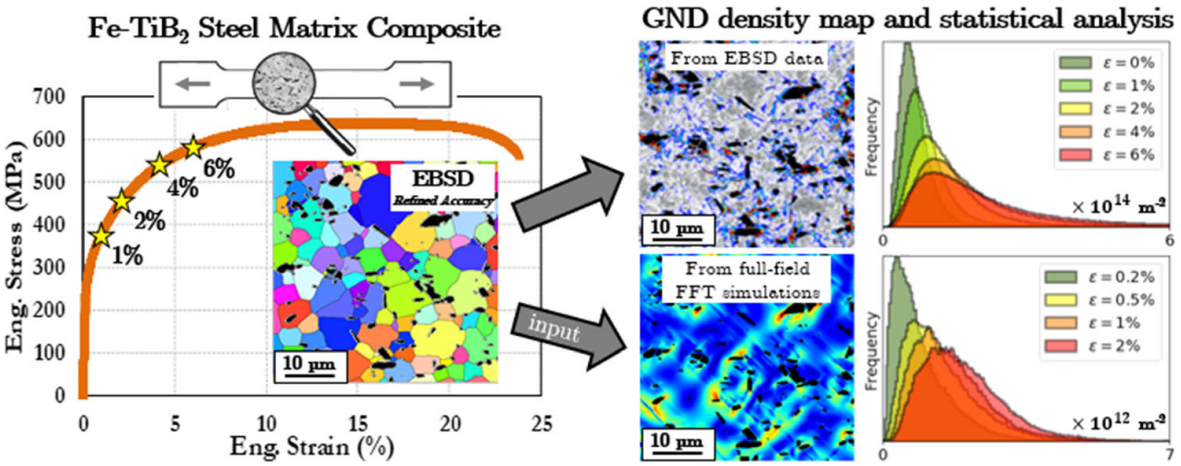

Introduction

Considerable efforts have been made to improve energy efficiency and reduce greenhouse gas emissions through the development of lightweight structures in the automotive industry. Ultrahigh resistance steels (dual phase, TRIP steels, etc.) were designed in order to allow thickness reduction in structural components [1]. However, this strategy has now reached its limits, given that, for some applications (such as chassis/suspension parts), further thickness reduction would result in a significant decrease in stiffness [2] and a subsequent increased risk for transportation security. A pertinent solution is to increase the specific stiffness (defined as E/ϱ) with addition of low-density and hard reinforcements in the steel matrix.

In this context, new ferrite steel matrix composites (SMCs) reinforced with titanium diboride (TiB_2) particles have been designed. Owing to the attractive properties of TiB_2 particles [3], the specific stiffness of Fe-TiB_2 SMCs with a 13% volume fraction of particles was shown to be significantly higher than for conventional steels [2, 4, 5]. Moreover, TiB_2 can be formed in situ from liquid melts during eutectic solidification. This is of great interest for industrial applications as it is compatible with the use of continuous casting and therefore ensures high productivity and low cost [2, 4].

However, few studies conducted on Fe-TiB_2 fabricated via in-situ solidification can be found in the literature. Most of them focus on the manufacturing process and its influence on the mechanical properties of the final product (see e.g., [6, 7]). Damage mechanisms have been investigated in samples subjected to simple shear [8], bending [9], monotonic tensile loading [10, 11], and more recently fatigue [12], but they are not yet fully understood. Plastic deformation of the matrix close to TiB_2 particles in the form of dislocation accumulation was suggested to play a key role in the mechanical strength of interfaces upon loading. Nonetheless, it was also reported to promote damage initiation [11]. The high dislocation densities at deformed TiB_2-ferrite interfaces were only evidenced through TEM observations in isolated configurations [13, 14]. These investigations suffer from a lack of statistics. Different microstructural features affect the plastic localization in a composite, e.g., the spatial distribution of particles or the matrix's grain size. To quantify their respective effect, large-scale characterizations are mandatory. Indeed, such studies at a mesoscopic scale are rather scarce in Fe-TiB_2 SMCs (and more generally in MMCs). They are yet necessary to infer the influence of the microstructure and to get a more complete understanding of collective plastic deformation mechanisms of the material. This is of major importance for industrial R&D to derive strategies toward microstructure optimization.

In this work, we present an experimental and numerical investigation to: (1) characterize at the mesoscale the localization of plastic deformation in

Fe-TiB_2 samples with increasing tensile deformation, and (2) quantify the effect of characteristic microstructural features of the composite. Electron back-scattered diffraction (EBSD) analyses and electron channeling contrast imaging (ECCI) were performed on samples deformed at different strain levels, with a special emphasis on the evaluation of geometrically necessary dislocations (GNDs) densities and their spatial distribution in the deformed microstructure. To our knowledge, such a study has not been performed yet on the considered material or any other steel matrix composite. The acquisition of accurate local orientation data in SMCs can be challenging, owing to the strong stiffness and hardening contrasts between steel and hard reinforcements leading to subsequent difficulties in material surface preparation [15–17]. In the present study, the estimated angular resolution was close to 0.1°, pushing conventional EBSD to its limits for this kind of material and allowing investigation of the first stages of plastic deformation.

Finally, we apply an enhanced elasto-viscoplastic fast Fourier transform (EVP-FFT) formulation [18], recently coupled [19, 20] with a phenomenological continuum mesoscale field dislocation mechanics (MFDM) theory [21–23]. The objective is to more correctly describe the spatial evolution of GND densities during straining of Fe-TiB_2. Contrary to conventional crystal plasticity, which only accounts for plastic flow and hardening induced by statistically stored dislocations (SSDs), MFDM-EVP-FFT also accounts for the evolution of GNDs and its effect on both plastic flow and hardening. In this contribution, realistic shape and distribution of TiB_2 particles derived from EBSD data acquired on the Fe-TiB_2 specimens is used as input of MFDM-EVP-FFT simulations in order to capture the observed influence of microstructural features on the distribution of GNDs in tensile-strained Fe-TiB_2.

Material and methods

Material

The Fe-TiB_2 SMC was obtained through in situ eutectic solidification as described in [4]. SMC sheets were then successively hot- and cold-rolled to reduce their thickness from 40 to 1.5 mm. A heat treatment at 1000 °C for 15 min was finally performed to achieve complete recrystallization of the α-Fe matrix. Table 1 shows the chemical composition of the as-received material.

The resulting microstructure is shown in Fig. 1 by means of an In-lens SEM micrograph (Fig. 1a) and an EBSD map (Fig. 1b). The ferrite grains are equiaxed in shape with an average size of about 4.5 μm. Their crystallographic texture evaluated from the EBSD data is relatively weak. The volume fraction of TiB_2 particles is about 9.5% (as evaluated by image analysis). While they seem to be uniformly distributed within the ferrite matrix at the large scale, many local configurations of agglomerated particles exist. Due to the processing route, TiB_2 particles are mainly elongated in the rolling direction (RD) and have a strong $< 0001 >$ //RD fiber texture (with the [0001] direction of the hexagonal lattice mainly aligned along RD). The particles have a mean area of about 1.2 μm^2 and a mean aspect ratio of 2.4 in the (RD, TD) plane. However, a large distribution in size and shape is observed, that is partly due to their fragmentation during cold rolling. Small voids separating these fragments of particles were filled with ferrite matrix in the course of rolling and subsequent thermal treatment.

Tensile tests

Four dog-bone tensile specimens machined out of SMC sheets were subjected to uniaxial tensile tests along RD. They were individually interrupted at ε = 1.0%, 2.1%, 3.9% and 6.0% of total strain to study the evolution of the deformation sub-structure with increasing strain level. The plastic strain was measured after unloading and ,respectively, equals to ε_p = 0.83%, 1.9%, 3.7% and 5.7%. As an illustration, Fig. 2 presents the typical engineering stress–strain response of Fe-TiB_2 SMC until failure.

EBSD analysis

Samples were extracted from the central part of the tensile specimens (as shown in red in Fig. 2). In order to get optimal surface quality for EBSD analysis, a specific polishing procedure was designed to deal with the strong stiffness contrast between ductile ferrite matrix and hard ceramic particles. The procedure consists of the following steps: a first grinding with resin bonded diamond discs (220 to 1200), a diamond polishing with polycrystalline suspension

Table 1 Composition of Fe-TiB_2 SMC in wt% (courtesy of ArcelorMittal Research)

Ti	B	C	S	N	0	Mn	Si	Cr	P	Al	Ni	Cu
5.48	1.73	0.022	0.0072	< 0.005	< 0.001	0.08	0.062	0.0829	0.0063	0.021	0.0149	0.02

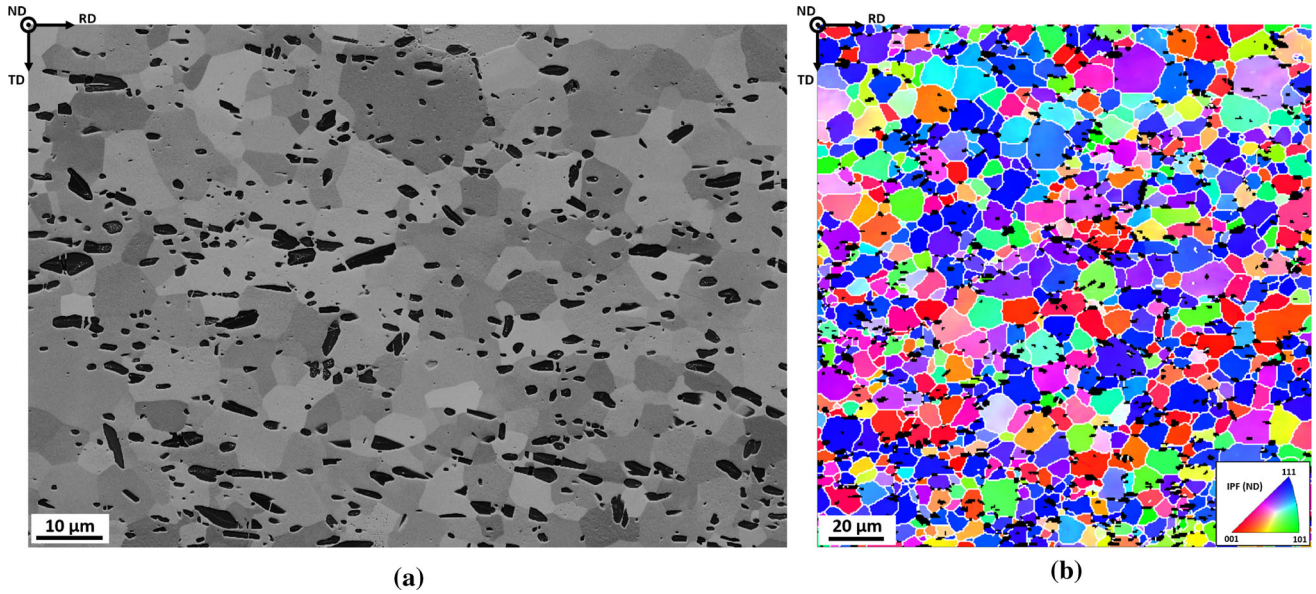

Figure 1 Microstructure of the as-received Fe-TiB_2 sheet: **a** In-lens SEM micrograph, **b** Inverse pole figure map of α-Fe (IPF//ND, grain boundaries with misorientation angles > 5° are plotted by white lines, the TiB_2 particles are colored in black).

Figure 2 Engineering stress–strain curve of the tensile test up to failure (red); four tensile specimens were individually loaded to the following plastic strains:ε_p = 0.83%, ε_p = 1.9%, ε_p = 3.7% and ε_p = 5.7%.

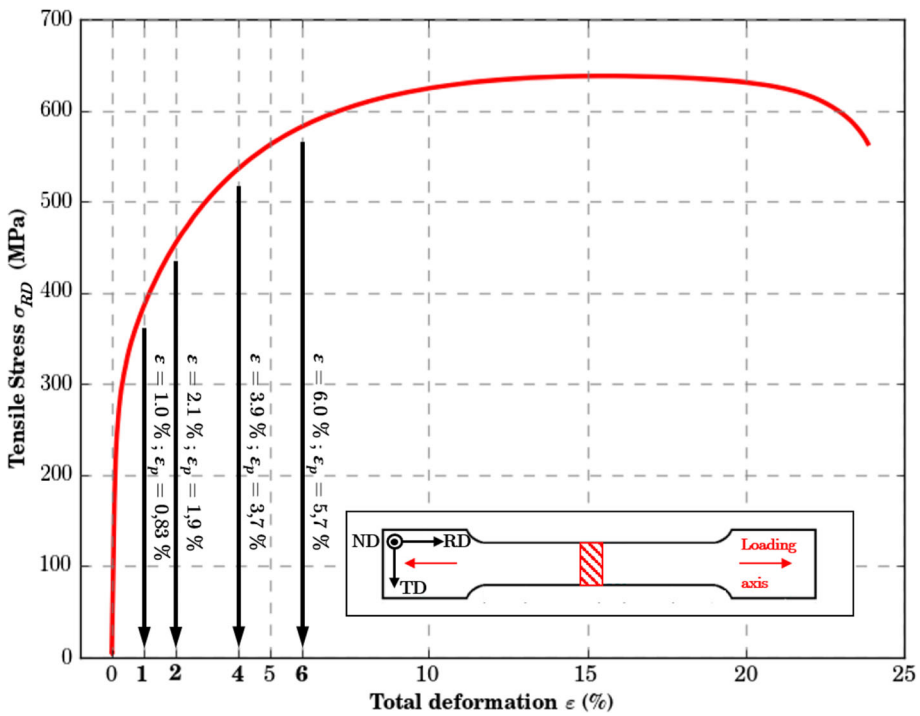

(9 to 1 μm), a final short polishing with a 0.02 μm non-crystallizing colloidal silica suspension with 30% H_2O_2 to eliminate any residual deformation induced by mechanical grinding.

EBSD maps were acquired using the CMOS-based *Symmetry* detector (full camera resolution: 1244 × 1024 pixels) and Aztec software from Oxford Instruments on a Zeiss Auriga 40 FEG-SEM at 20 kV, 70° tilt and 8 mm working distance. High -resolution patterns were acquired in 2 × 2 data binning and processed in "refined accuracy" mode [24]. The global speed was around 55 Hz. Each map was acquired with a step size of 100 nm. This setting has been optimized to cover large areas with a satisfying spatial resolution and an improved angular resolution of the orientation data. Three maps covering each around 200 grains were scanned over each specimen in order for data to be statistically representative of the microstructure for each level of plastic strain. The indexing rate was always superior to 97%.

In order to quantify plastic deformation and its localization in the Fe-TiB_2 deformed microstructure, EBSD-based parameters are calculated from each EBSD scan data. In the following sections, our study focuses on the spatial distribution of GND densities measured for each pixel and their evolution with plastic strain. All calculations and analyses of EBSD orientation maps were performed with the ATEX software [25]. The components of the lattice curvature tensor $\boldsymbol{\kappa}$ are derived from the orientation gradients between a pixel of the map and the neighboring pixels. The components of the Nye dislocation density tensor $\boldsymbol{\alpha}$ are then determined as indicated in [26]. When neglecting the contribution of elastic strains, they can be expressed as follows:

$$\alpha_{ij} = \kappa_{ji} - \delta_{ji}\kappa_{kk}$$

where δ_{ji} is the Kronecker delta with i, j = 1, 2, 3 and $\kappa_{kk} = \kappa_{11} + \kappa_{22} + \kappa_{33}$. As out-of-plane curvatures are not accessible in conventional 2D EBSD (the plane of investigation is here represented by directions x_1 and x_2), only the six components κ_{j1}, κ_{j2} can be obtained. Therefore, five of the nine components of the tensor $\boldsymbol{\alpha}$ are then calculated: α_{12}, α_{13}, α_{21}, α_{23} and α_{33} (i = 1,2 and 3 denoting RD, TD and ND, respectively, as reported on Fig. 1). The GND scalar density is finally estimated using the L^1 norm of the Nye tensor. It should be noted that a threshold misorientation angle of 5° between two measurement pixels was considered for the calculation of the GND density.

FFT-based mesoscale field dislocation mechanics (MFDM): MFDM-EVP-FFT

A MFDM-EVP-FFT model is used in order to capture the evolution of GND densities and the effects of microstructural features on the spatial distribution of plastic deformation, showing good agreement with observations of the strained Fe-TiB_2 samples. The model is applied to micromechanical simulations of Fe-TiB2 under tensile loading instantiated from EBSD images. The MFDM theory was introduced by Acharya and co-workers [27–30] and builds upon conventional crystal plasticity models by taking into account the evolution of GNDs at the mesoscopic scale, as well as their effect on local stress field, plastic strain rate and strength of the material. To that end, the Nye's dislocation density tensor $\boldsymbol{\alpha}$ is used as an internal variable. The crystal plasticity elasto-viscoplastic FFT formulation first reported by [18], denoted here as CP-EVP-FFT here, has been extended by [19, 20, 31] to consider MFDM equations in its reduced version [22]:

$$\begin{aligned} div\ \boldsymbol{\sigma} &= 0 \\ \boldsymbol{\sigma} &= \boldsymbol{C} : (\boldsymbol{U^e})^{sym} \\ \boldsymbol{U} = grad\ \boldsymbol{u} &= \boldsymbol{U^e} + \boldsymbol{U^p} \\ \dot{\boldsymbol{U}}^{\boldsymbol{p}} &= \boldsymbol{\alpha} \times \boldsymbol{v} + \boldsymbol{L^p} \\ \dot{\alpha} &= -curl\left(\dot{\boldsymbol{U}}^{\boldsymbol{p}}\right) \end{aligned} \tag{2}$$

where $\mathbf{u}$ is the displacement field, $\boldsymbol{\sigma}$ is the Cauchy stress tensor, $\mathbf{U^e}$ and $\mathbf{U^p}$ are the elastic and plastic distortion tensors respectively, $\boldsymbol{\alpha}$ is the dislocation density tensor (the Nye tensor), $\mathbf{v}$ is the GND velocity vector, $\mathbf{L^p}$ is the plastic distortion rate due to SSD mobility, The curl, div and × symbols denote the curl, the divergence and the cross product operators, respectively. Periodic boundary conditions are used, see [32, 33]. Equation (2) represent the main field equations of the MFDM theory. The scalar GND density is then computed from the Nye tensor components as:

$$\rho_{GND} = \sqrt{\alpha : \alpha}/b \tag{3}$$

For the sake of conciseness, the technical details of the MFDM-EVP-FFT numerical implementation are not reported here, but can be found in our previous works [19, 20, 31].

Input data

Input microstructures for the numerical simulations are obtained from EBSD data acquired on Fe-TiB_2 specimens. A $512 \times 512 \times 1$ two-phase voxelized unit cell is built up from each acquired EBSD map, made of purely elastic particles embedded in a single crystal elasto-viscoplastic matrix with specific crystallographic orientations. Assumption of anisotropic linear elastic behavior for particles is consistent with the strong elastic stiffness contrast with the ferrite matrix. A single-crystal ferrite matrix is considered in order to focus the discussion on the effect of particle features only, and to put into evidence the superior capability of MFDM-EVP-FFT over the conventional CP-EVP-FFT to describe accumulation of GNDs at the particle/matrix interface. Two crystallographic orientations for ferrite are considered, in order to provide some qualitative insight of the effect of the local crystallographic orientation on the distribution of GND densities. The first one is associated with multiple slip and such that $[\underline{1}\underline{1}\underline{1}]$ lies parallel to the tensile direction. For the second crystal orientation, with $[\underline{5},\underline{6},\underline{27}]$ parallel to the tensile direction, single slip is the preferred slip mode (with $(\underline{1}\underline{1}\underline{2})[\underline{1}\underline{1}\underline{1}]$ system exhibiting the highest Schmid factor). These orientations will be referred to as orientation #1 and orientation #2, respectively.

Elastic constants for the ferrite matrix and the particles are reported in Table 2. These reflect the linear anisotropic elastic behavior of TiB_2 with hexagonal symmetry, which is considered to be transversally isotropic, and the linear elastic behavior of α-ferrite, which is assumed to be isotropic. For the elasto-viscoplastic matrix, the constitutive parameters related to slip and GND velocity are consistent with pure α-Fe, and are identical to the ones reported in a previous work [31].

Given the body-centered cubic structure of α-Fe lattice, both $\{110\}\bar{1}11$ and $\{211\}\bar{1}11$ slip systems are considered (i.e., a total of 24 slip systems). The simulation cell is subjected to a pure uniaxial tensile loading in RD as in experimental tests, with mixed strain/stress boundary conditions and an applied strain rate $\dot{E}_{RD} = 0.001\ s^{-1}$.

Experimental results

Orientation data precision

For GND density analysis at low deformation level, it is of major importance to evaluate the angular resolution of our EBSD data. Even if there is no universal agreement in the literature, this quantity is often compared with the kernel average misorientation (KAM) angle distribution corresponding to the undeformed material [35, 36].

Figure 3 presents the distribution of the KAM angle derived from raw orientation data acquired on the Fe-TiB_2 undeformed sample, showing impressively low values for such complex composite material. Indeed, the average KAM angle and its 95th percentile are respectively of 0.069° and of 0.12°. Typically, the angular resolution of conventional Hough-transform-based EBSD analysis is about 0.5–1°, depending on the material and the EBSD acquisition settings [37]. In this study, the angular resolution is significantly better thanks to three experimental improvements: the high resolution of the EBSD patterns, the use of the "refined accuracy" (RA) mode, and an optimal surface preparation. Previous studies have already demonstrated an improved EBSD precision using RA mode. In [36], the grain-average KAM angle in recrystallized Inconel 718 grains was shown to decrease from about 0.5° to about 0.1°. Similar conclusions were reached in [38] in undeformed UO_2 pellets. In the present paper, the angular resolution is further improved as the 95th percentile of KAM angle distribution (θ_{95}) is close to 0.1°. In our opinion, the effective angular resolution could even be lower. Indeed, local misorientations measured in the strain-free sample may be induced by residual deformation around particles due to the difference in thermal expansion between ferrite and TiB_2 particles during final cooling. To a lesser extent, it may be due to residual

Table 2 Elastic constants used for numerical simulations (from [34])

TiB_2 (HCP)					Fe-α (BCC)	
C_{11}(GPa)	C_{12}(GPa)	C_{13}(GPa)	C_{33}(GPa)	C_{44}(GPa)	E(GPa)	ν
654.5	56.5	98.4	454.5	263.2	211	0.33

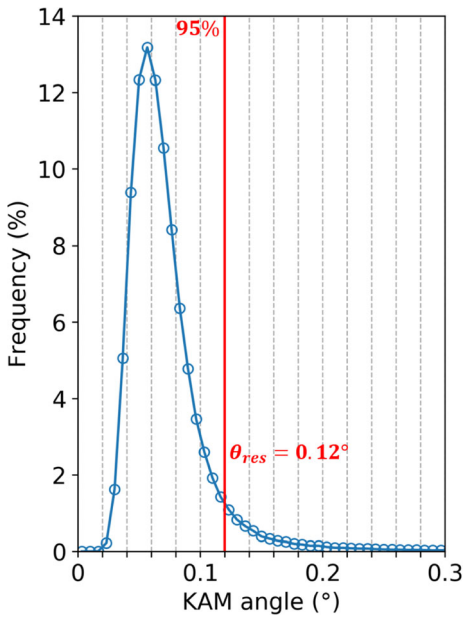

Figure 3 KAM-angle distribution derived from EBSD data acquired on the undeformed Fe-TiB_2 sample. The average KAM is of 0.069° and its 95th percentile: $\theta_{95} = 0.12$ °.

surface scratches induced by mechanical polishing. The precision of orientation measurements could be further increased with the use of techniques such as pattern matching [35, 36, 39] or High-Resolution EBSD (HR-EBSD) [40, 41]. However, these techniques are still not adapted to large EBSD datasets.

Statistical analysis of GND density evolution during plastic deformation

Owing to the low orientation noise of the EBSD data performed for each deformed sample, the evolution of GND density can be captured in the Fe-TiB_2 composite at the early stages of plasticity, during the elasto-viscoplastic transition. Figure 4a quantifies the evolution of GND density with plastic strain. The observed increase in GNDs within the material is expected to maintain strain compatibility.

For further statistical analysis, these data were fitted with a log-normal probability density function, and the mean and variance of the distribution of each deformed state were obtained. Also, we ensured that the EBSD maps provide statistically representative data. Firstly, it was checked that the distributions of GND densities did not vary significantly between the three maps acquired on the same sample. Secondly, the evolution of mean $\overline{\rho}_{GND}$ was calculated as a function of the number of considered grains, as done in [42]. Figure 4b indicates that about 100 grains are necessary for statistical significance regarding the mean value: $\overline{\rho}_{GND}$. This number increases slightly with the deformation level, suggesting an increase in heterogeneity in the spatial distribution of GND densities. In any case, the investigated number of grains was always higher than this minimum.

The mean GND density extracted from measurements on the undeformed specimen is used as a measure of the GND noise floor: $\rho_{NF} = 7.06 \times 10^{13}$ m^{-2}. The uncertainty δ in the orientation measurement can be retrieved by $\rho_{NF} = \delta/b\Delta x$ [43], where b is the Burgers vector's magnitude (0.248 nm for α-Fe) and Δx is the step size of the EBSD map. This leads to $\delta \sim 0.1°$ which comforts the previous estimation of our orientation data precision (see Sect. 3.1). The fraction of measured GND densities that fall below the noise floor, i.e., such that $\rho_{GND} < \rho_{NF}$ is found to decrease in deformed specimens with increasing plastic strain and is evaluated at $\cong 53\%$ for $\varepsilon_p = 0.83\%$, $\cong 27\%$ for $\varepsilon_p = 1.9\%$, and finally $\cong 15\%$ for $\varepsilon_p = 3.7\%$ and $\varepsilon_p = 5.7\%$. This fraction is still non-negligible for the lowest deformed sample, suggesting that further improvement in orientation precision would be required for investigation of very low strains ($\leq 1\%$).

Interestingly, the mean GND density increases linearly with ε_p at least up to 5.7% (see Fig. 5a). This indicates that the storage of GNDs is a macroscopic signature, even if GND densities develops due to microstructural features such as particles or grain boundaries. Similar trends were observed for an IF steel by [44] for the evolution of the quantity GOS/D (where GOS is the Grain Orientation Spread and D is the grain size) as a function of tensile deformation at small strains up to 7%. This conforms to Ashby's model [45] for plastically non-homogeneous polycrystals for which the GND density is proportional to the plastic strain and can be expressed as:

$$\rho_{GND} = \frac{\varepsilon_p}{4b\lambda} \tag{4}$$

where b is the magnitude of the Burgers vector and λ is an average slip distance for dislocations, usually taken as the average grain size. Accounting for both average grain size D and particle interspacing p, the GND density expression can be modified considering the relation $1/\lambda = 1/D + 1/p$. The average particle interspacing is approximated to $p = 1.47$ µm using simplified relation from [46]. For a plastic strain of

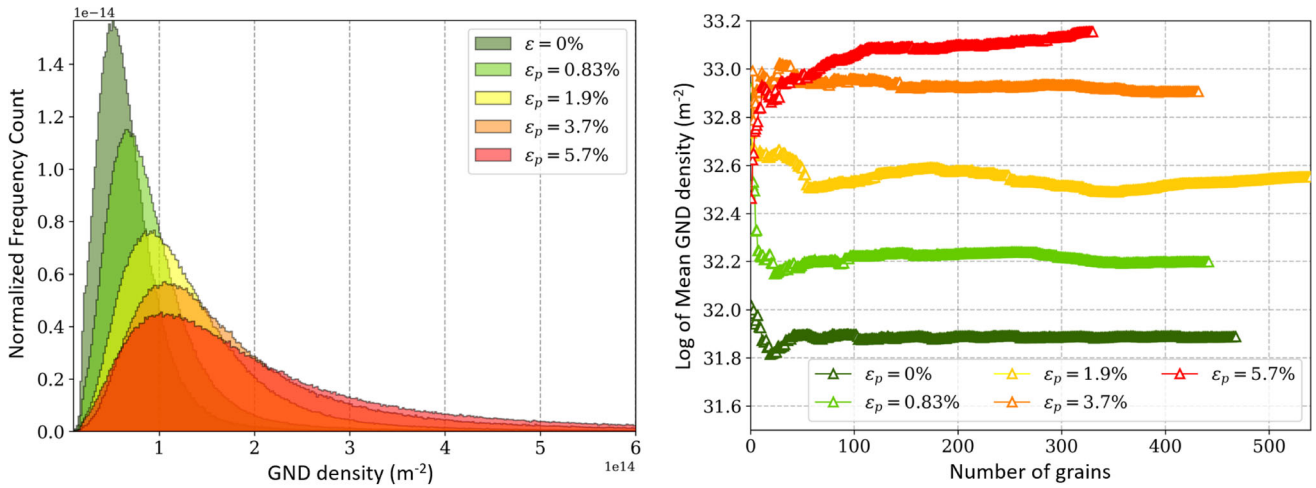

Figure 4 **a** Distribution of GND densities for specimens deformed with increasing plastic strain up to 5.7%; **b** Log of mean GND density as a function of the number of grains considered.

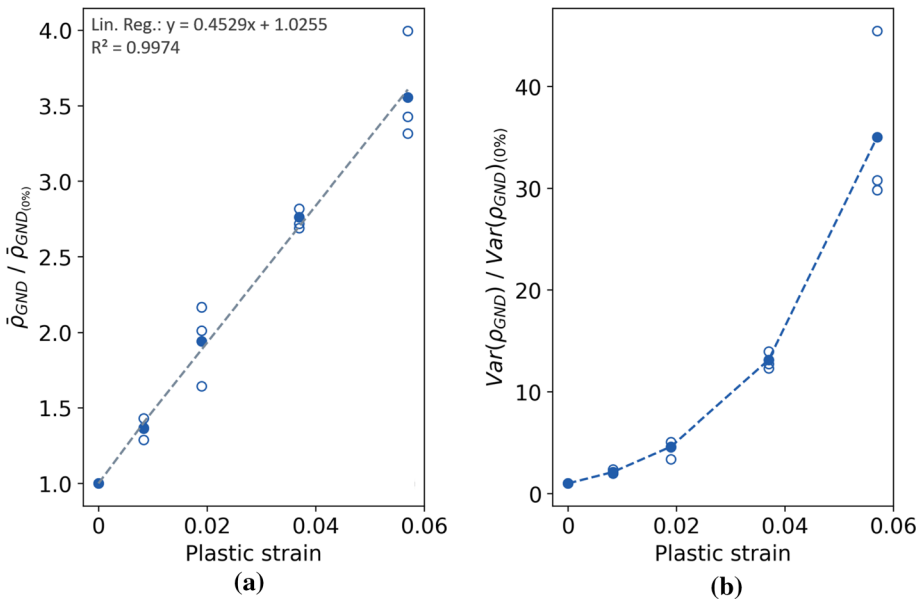

Figure 5 Evolution of **a** the mean GND density $\overline{\rho}_{\mathrm{GND}}$ (normalized by the mean GND density of the undeformed sample $\overline{\rho}_{\mathrm{GND},(0\%)}$ and **b** the variance of the GND density as a function of the overall plastic strain.

5.7%, the estimated GND density is then $\rho_{\mathrm{GND}} = 5.18 \times 10^{13}$ m^{-2}, which is one order of magnitude lower than experimental value. The discrepancy in results can be explained as follows. Firstly, the hypotheses of Ashby's model are oversimplified. Secondly, the GND density estimated from EBSD data is definitely not the true absolute value of GNDs as it is highly dependent on the acquisition conditions.

The variance of GND density is more sensitive to spatial correlations of GND densities. Its increase as a function of ε_p(depicted in Fig. 5b) is coherent with the development of non-uniform distributions of GND densities throughout the microstructure and becomes very significant for $\varepsilon_p > 2\%$. Here, no saturation of GND density was observed up to 6% of plastic strain. It could be expected at higher strains ($\varepsilon > 10\%$) when SSDs, developing mostly in the bulk of grains, progressively exceed GNDs in quantity, as was observed in polycrystalline copper [47] and nickel [48].

Spatial distributions of GND density in relation to microstructural features

Figure 6 shows one of the three GND density maps acquired for each deformed state. Consistent with previous statistical results, the progressive development of heterogeneous deformation structures was observed with increasing tensile strain. At ε_p = 1.9%, most high-density GND pile-ups are formed close to TiB_2 particles (Fig. 6b). Sub-boundaries disoriented between 1° and 5° start to develop in the vicinity of TiB_2 particles while a network of lower angle sub-boundaries (< 0.5°) expands inside the grains. From ε_p = 3.7%, GND pile-ups significantly increase both in number and intensity (Fig. 6c-d). Dislocation cell arrangements are observed in some grains (ρ_{GND} = 2 to 3 × 10^{14} m^{-2} in cell walls, ρ_{GND} = 8 × 10^{13} to 1.5 × 10^{14} m^{-2} in cell interiors) while most intense GND pile-ups (ρ_{GND} = 5 × 10^{14} to 1 × 10^{15} m^{-2} and higher) develop from particles and expand into the matrix with wavy paths. Some GND pile-ups are also formed inside ferrite grains, apparently far from any visible particle, or along grain boundaries. GND walls thicken and have more branches as deformation increases. With increasing strain level (ε_p > 3.7%), already existing sub-boundaries present in grains and close to particles reach higher disorientation values whereas the low angle sub-boundaries network (< 0.5°) does not further extend. Interestingly, the largest GND pile-ups are observed

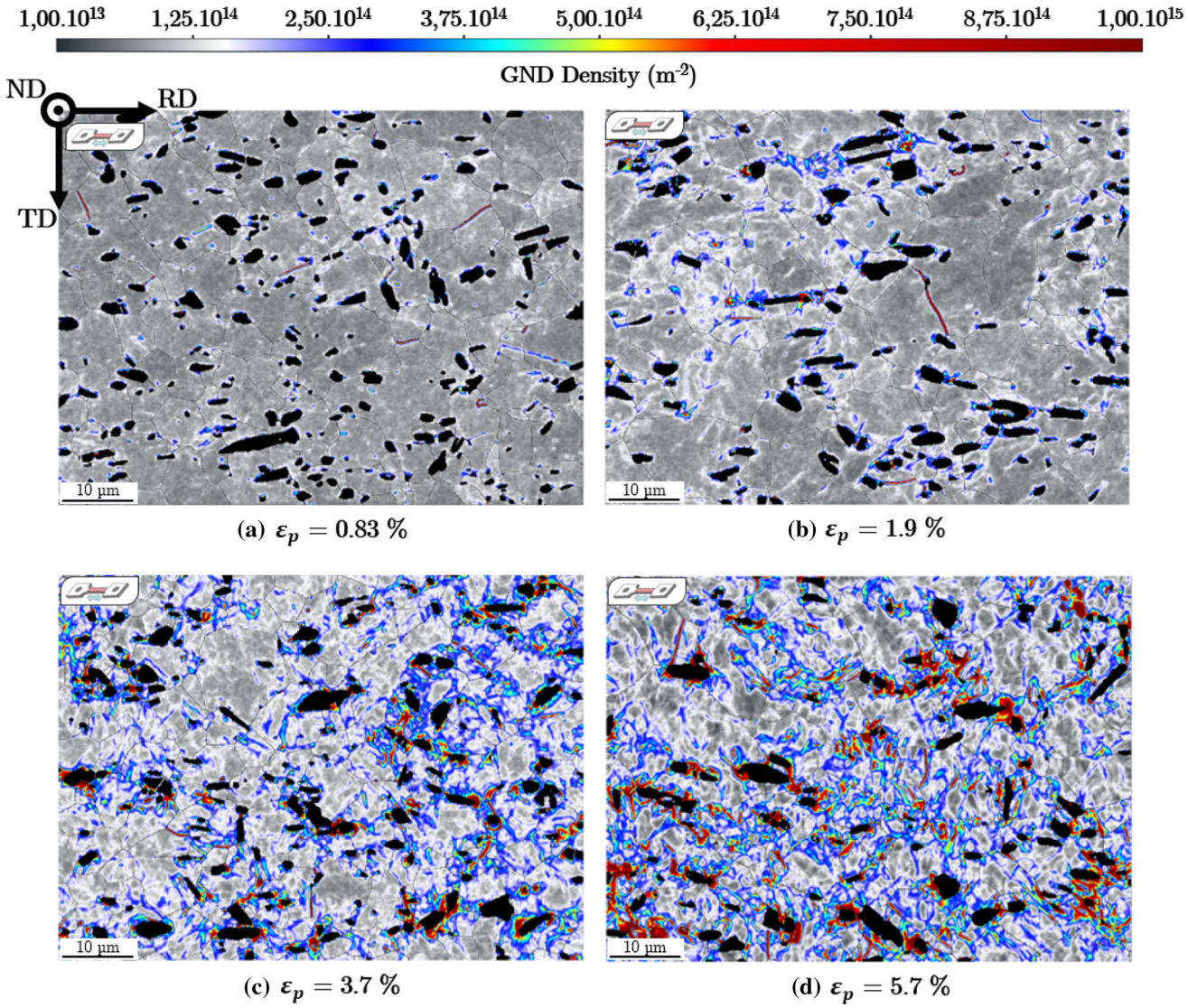

Figure 6 GND density maps of specimens deformed at: **a** ε_p = 0.83%, **b** ε_p = 1.9%, **c** ε_p = 3.7% and **d** ε_p = 5.7%.

close to particles that are packed together (see Fig. 6d), suggesting an effect of particle clustering on the localization of plastic deformation.

For elongated particles, high GND densities appear to be mainly located at particle's tips showing a particle shape effect on GND density pile-ups. Both the particle clustering and shape effect on localization of plastic deformation are further analyzed in Sect. 3.4. No apparent correlation between particle size and GND density can be evidenced: GND hot-spots are found close to large as well as small particles. Some intense GND walls are located at ferrite grain boundaries. This suggests that the spatial distribution of GNDs is also affected by the crystallographic misorientation between ferrite neighboring grains.

Figure 7 presents a GND density map derived from EBSD data obtained at the surface of the sample strained at $\varepsilon_p = 3.7\%$, together with ECCI micrographs in selected regions. Channeling contrast at 0° tilt is used here to reveal the arrangement of dislocations close to the surface. Abrupt orientation contrast variations are observed, consistent with the organization of high-density GNDs in walls and cells inside the deformed microstructure. Individual grouping of dislocations in cells can be evidenced inside ferrite grains and dislocations are also observed to pile-up close to particle interfaces. Dislocation substructures like tangles are observed to emanate mainly from particle tips (and particle edges in a more general case, see yellow arrows in Fig. 7c, e) and often appear to be constrained in the channels separating neighboring particles. This is concomitant with the previous observations regarding higher GND densities evaluated in clusters of particles. The high BSE contrast observed at the matrix/particle interface is attributed to a locally higher amount of dislocations but also to a local change in surface topography, which makes identification of dislocation pile-ups more delicate in this region.

In the maps of Fig. 6, locally higher GND density walls were observed inside ferrite grains with no visible neighboring particle or grain boundary. Such regions were further imaged in BSE mode at high accelerating voltage (enabling a larger interaction volume). As shown in Fig. 8, these high GND densities, particles were systematically observed deeper in the volume of the grains, whereas they were not detected on the EBSD map (green frame). In addition, GND pile-ups observed at the surface and extending from a particle into the neighboring ferrite matrix could be attributed to the 3D morphology of the same particle (red frame). Thus, it should be kept in mind that 2D maps of orientation data are subjected to a "3D microstructural effect" or "long-range effect" of underlying particles that introduce a bias in statistical analysis derived from 2D maps.

Influence of microstructural features: particle spacing and morphology

Qualitative analysis of GND maps has shown that GNDs tend to accumulate mostly near interfaces between ferrite matrix and TiB_2 particles (see Fig. 6). A more quantitative insight of the correlation between specific microstructural features and the localization of GND pile-ups is presented next. Four microstructural length scale parameters have been calculated from EBSD maps: the distances to the closest (a) TiB_2 particles (d_{CP}), (b) ferrite grain boundaries, (c) particle tips, (d) ferrite triple points (pixels where three of more ferrite grains do meet).

The methodology is detailed for the case of closest particles, and can be easily extended to the other features. From each EBSD map, Euclidian distance between each pixel in the ferrite phase and the closest particle (d_{CP}) were calculated. Figure 9a reports the d_{CP}-map calculated from the EBSD map of the sample strained at $\varepsilon_p = 3.7\%$ (Fig. 6c). It is easily observed that high values of d_{CP} (blue regions) correspond to regions with high particle interspacing. On the other hand, lower values are mostly obtained in regions where particles are packed together. Therefore, d_{CP} also quantify the particle interspacing effect. Finally, ferrite regions far or close to particles (respectively Region 0 and 1) are differentiated for further analysis of the corresponding GND densities (as shown in Fig. 9b). The threshold value for high and low d_{CP} distances is always 1 μm in the study.

For statistical analysis of internal length effects, we averaged the measured GND densities in both regions 0 and 1 for each map and for each plastic strain level. The result is given in Fig. 10. Irrespective of the plastic strain level and the considered distance, the GND density is always higher in regions 1 than in regions 0 ("red on top of blue"). This is a result, as expected, of particles, grain boundaries, particle tips and triple points, all acting as barriers to dislocation motion. In particular, more intense GNDs are found

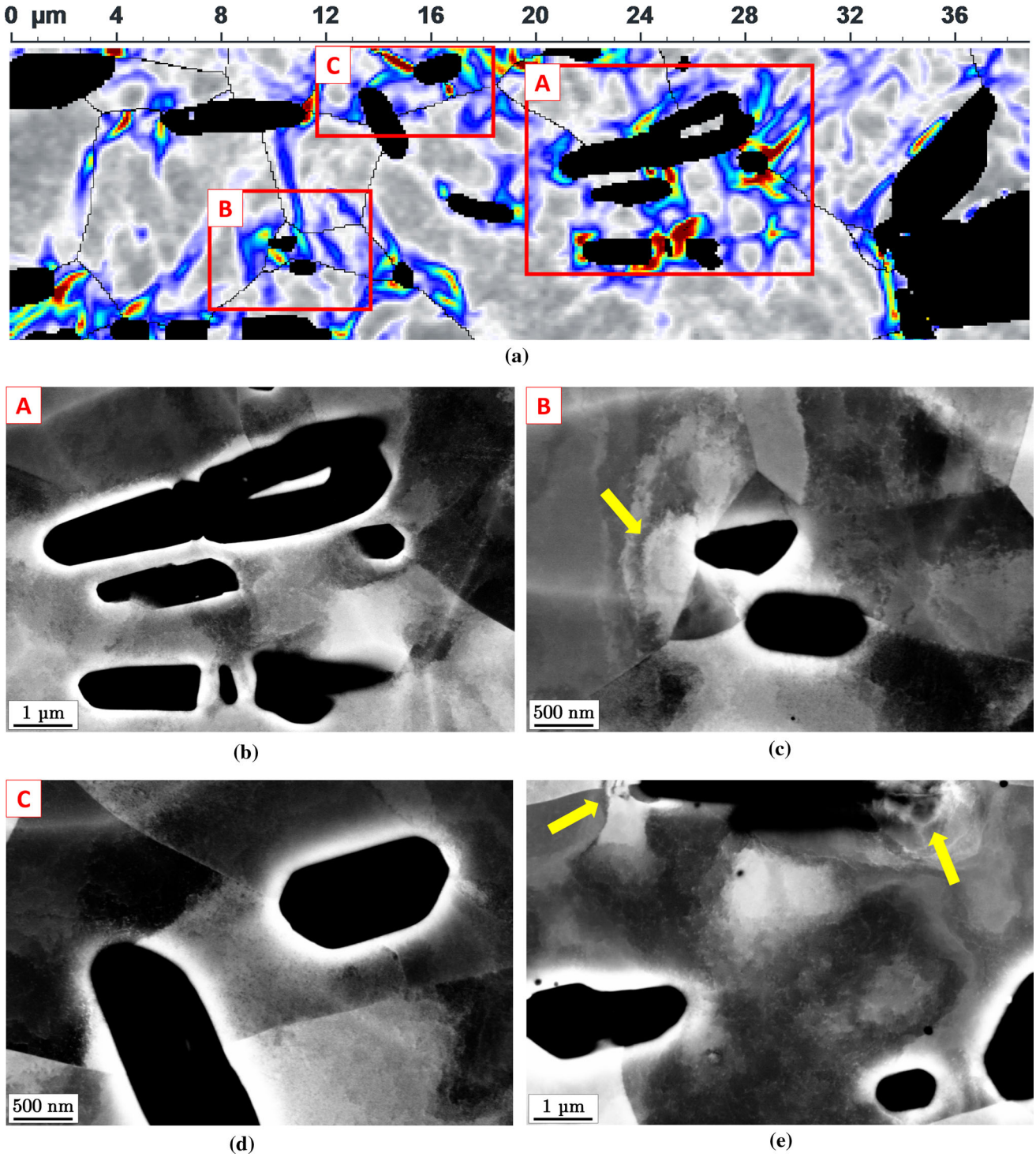

Figure 7 **a** Crop of the GND density map of the 3.7% deformed specimen (the scale is the same as in Fig. 6). Red boxes labeled A, B and C indicate regions of interest further imaged by ECCI in **b**, **c** and **d**. The ECCI micrograph in **e** was taken from the 5.7% deformed sample.

for low particle interspacing as was qualitatively observed in the maps of Fig. 6. In addition, the mean GND densities increase with plastic strain both in regions 0 and 1. However, the increase in average GND density is found to be significantly higher for low particle interspacing and close to particle tips (Fig. 10a, c) than near grain boundaries and triple points (Fig. 10b, d). In regions far from

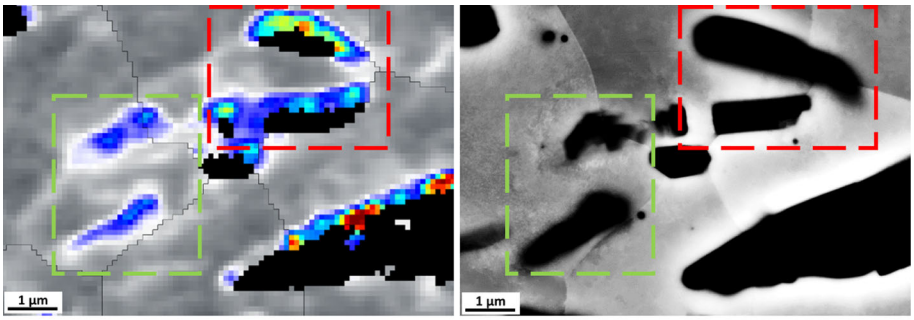

Figure 8 **a** GND density map of the 0.83% deformed specimen and **b** associated high magnification BSE image at 30KV.

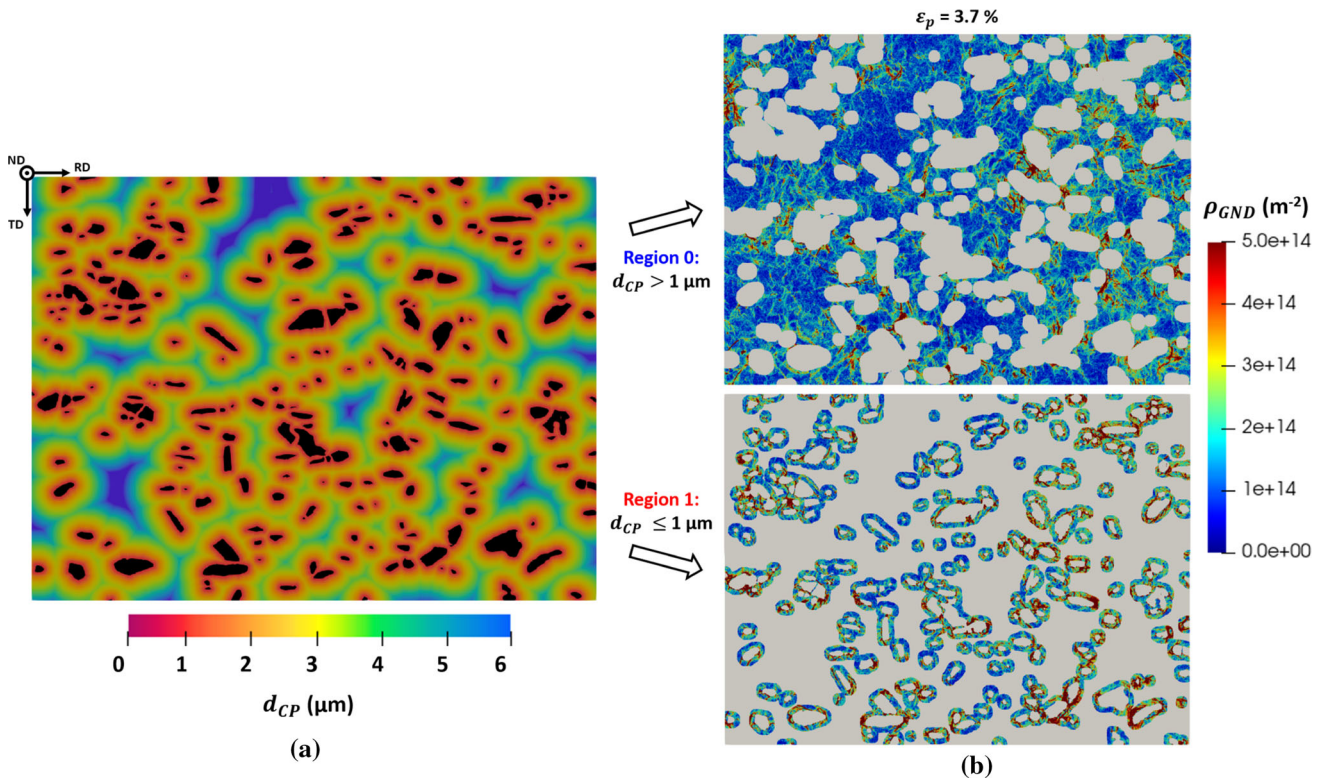

Figure 9 **a** d_{CP}-map of the distance to the closest particle (µm) calculated from the EBSD map of the 3.7% strained sample (**Fig. 6c**); (b) GND map of Region 0 where $d_{CP} > 1$ µm and Region 1 where $d_{CP} \leq 1$ µm.

microstructural features (blue curves), the slope conforms to the average evolution of GND density as a function of plastic strain reported on 3.2 (see dotted grey line). When considering regions close to particles (regions 1 in Fig. 10a, c), the slope is significantly higher, suggesting a reduced average slip distance for dislocations within these regions. It was checked that the latter result is independent of the threshold distance used to differentiate regions 0 and 1. Thus, it is inferred that the particle interspacing is more detrimental to plastic strain localization than the ferrite grain size.

The preferential accumulation of GNDs with strain near particle tips shown in Fig. 10c confirms the effect of particle morphology on plastic deformation localization. Indeed, higher average GND density is found close to tips of elongated particles, especially for $\varepsilon_p \geq$ 3.7%, than along all the particle/matrix interfaces. Comparison of Fig. 10 b, d shows that more GNDs are found at ferrite triple junctions than at grain boundaries; it is, however, a less pronounced phenomenon.

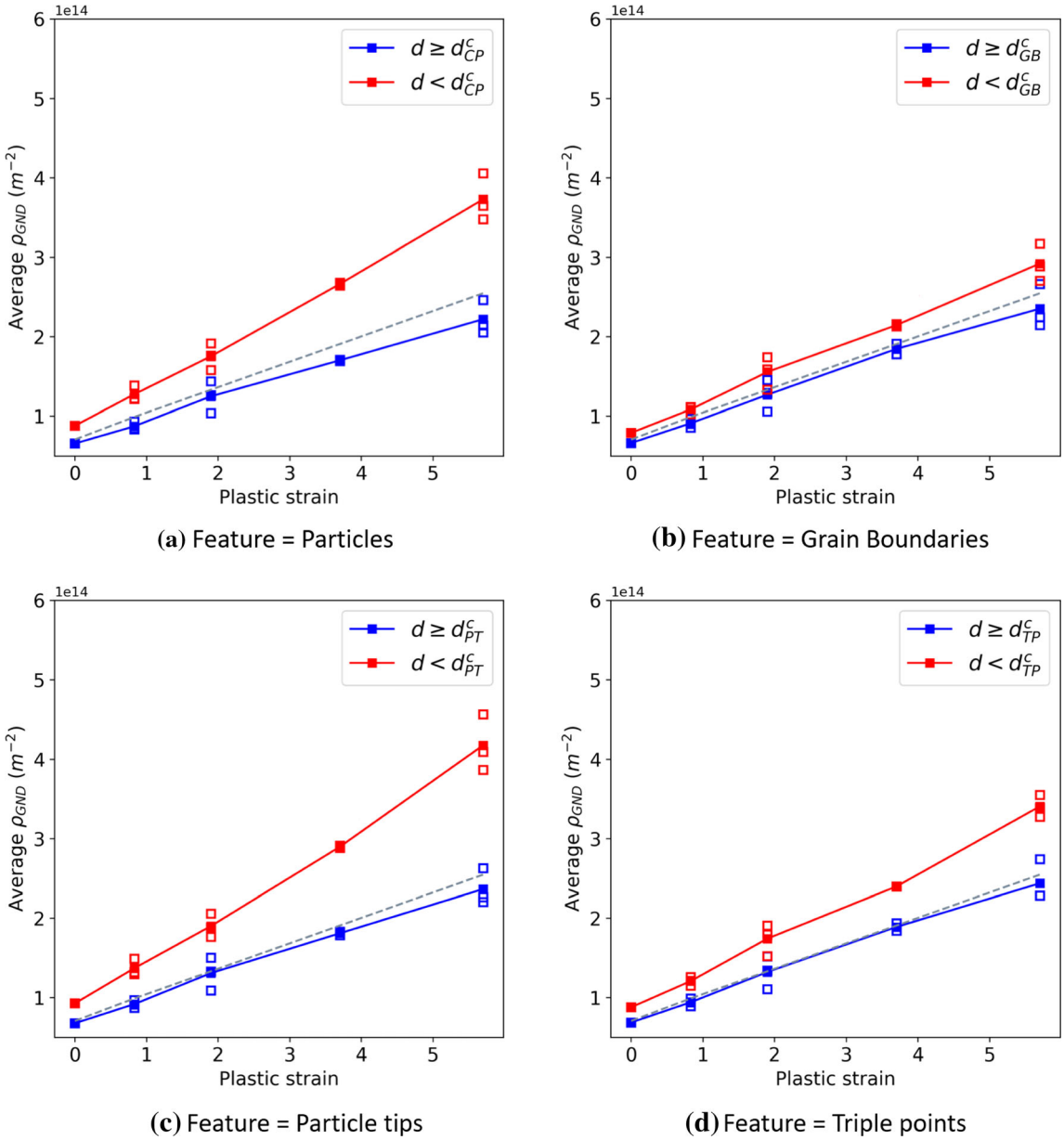

Figure 10 Evolution with plastic strain of average GND densities in regions far from ($d >$ 1 µm, blue curves) and close to microstructural features ($d \leq$ 1 µm, red curves), where considered features are respectively: **a** particles, **b** grain boundaries, **c** particle tips, **d** triple points. The grey dotted line corresponds to the average evolution of GND density from Fig. 5a.

MFDM-EVP-FFT simulation results

The MFDM-EVP-FFT model is now applied to simulate the statistical evolution of the GND density with increasing strain and capture local variations induced by microstructural features of the TiB_2 particles as observed experimentally. Details of the model are recalled in Sect. 2 and input data in 2.5. The MFDM-EVP-FFT simulations are always compared to conventional crystal plasticity CP-EVP-FFT simulations.

Statistical evolution of simulated GND density with strain

The statistical distributions of GND densities with increasing strains predicted by MFDM-EVP-FFT and by CP-EVP-FFT are reported on Fig. 11a-b. The input microstructure is obtained from all EBSD maps

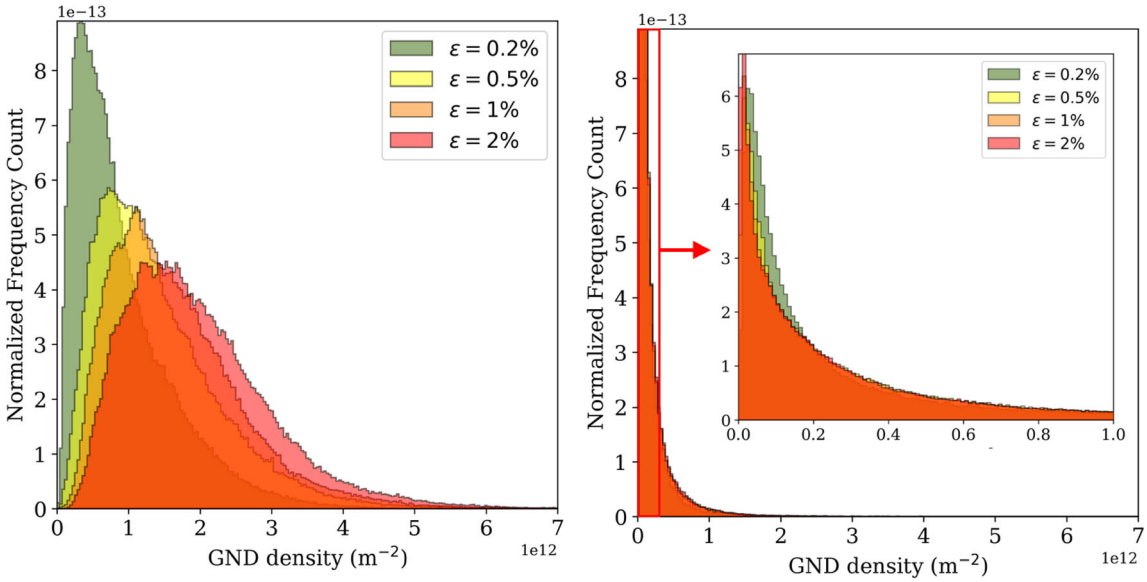

(a) MFDM-EVP-FFT **(b)** CP-EVP-FFT

Figure 11 Distribution of GND densities ρ_{GND} for MFDM-EVP-FFT (a) and CP-EVP-FFT (b) simulations at different macroscopic strains: ε = 0.2% (green), ε = 0.5% (yellow), ε = 1% (orange) and ε = 2% (red). The input microstructure is obtained from all EBSD considering a single-crystal ferrite matrix of orientation #1.

considering a single-crystal ferrite matrix of orientation #1 (see Sect. 2.5). Interestingly, the MFDM-EVP-FFT simulations (Fig. 11a) reproduce the experimental trends (Fig. 4a). Indeed, with increasing macroscopic strains, broader distributions centered at increasing values of ρ_{GND} are obtained. Similar trends are obtained for orientation #2. In contrast, CP-EVP-FFT simulations (Fig. 11b) are not satisfying. The values of ρ_{GND} are approximately 2 orders of magnitude lower than the MFDM-EVP-FFT values. With increasing strains, the distribution remains centered at very low values of ρ_{GND}. This is qualitatively inconsistent with experimental data given in Fig. 4a.

As a result, the predictions given by the MFDM-EVP-FFT model are more realistic than the ones given by conventional crystal plasticity. The simulated GND densities remain lower than those measured by EBSD. However, their evolution with increasing strain reproduces well the experimental trends. One has to keep in mind that the absolute value of GND density measured by EBSD is also questionable as it is greatly influenced by the orientation noise and the step size [49]. In any case, MFDM-EVP-FFT gives more relevant qualitative distributions than CP-EVP-FFT.

Spatial distributions of GND density in relation to microstructural features of particles

Figure 12 displays the spatial distributions of GND density ρ_{GND} simulated with MFDM-EVP-FFT and compared to CP-EVP-FFT for orientations #1 and #2 of the ferrite matrix at two macroscopic strains: ε = 0.2% and ε = 2%. MFDM-EVP-FFT simulations successfully predict the localization of plastic deformation at particle/matrix interfaces (Fig. 12a, e). As macroscopic strain increases (Fig. 12b, f), the simulations capture the progressive accumulation of GNDs in pile-ups extending inside the neighboring matrix. In contrast, CP-EVP-FFT simulations completely underestimate this heterogenous spatial distribution. GND densities are very low in magnitudes and are purely interfacial. Indeed, the GNDs remain in thin layers constrained at particle/matrix interfaces with increasing macroscopic strain (Fig. 12c, d, g, h). Conventional crystal plasticity is unable to qualitatively describe the development of GND pile-ups that spread in the surrounding matrix. In addition, simulated ρ_{GND} are 1–2 orders of magnitude lower than in the case of MFDM-EVP-FFT simulations.

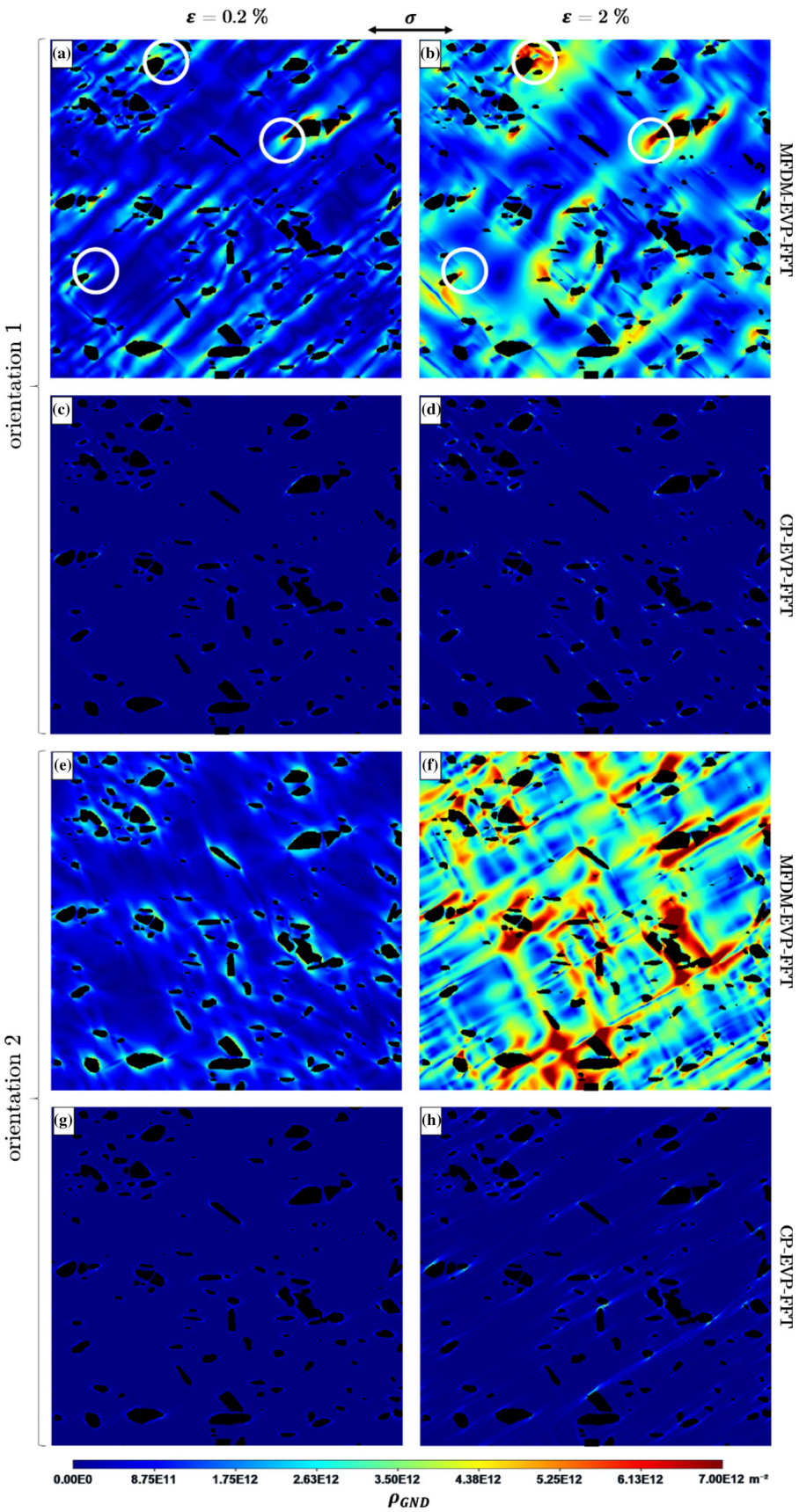

Figure 12 Spatial distributions of GND density ρ_{GND} predicted with MFDM-EVP-FFT and compared to CP-EVP-FFT (conventional plasticity) for macroscopic strains $\varepsilon = 0.2\%$ and $\varepsilon = 2\%$ and two crystallographic orientations of the ferrite matrix. Orientation #1 is such that $[\bar{1}11]$ lies parallel to the tensile direction (multiple slip). For orientation #2, $[\bar{5}, 6, 27]$ is parallel to the tensile direction (single slip).

The MFDM-EVP-FFT simulations also predict the preferential accumulation of GNDs at particle tips, experimentally observed in Sect. 3.3 (Fig. 6). These white circles in Fig. 12 (a, b) highlight some typical GND configurations at particle tips for orientation #1. This shape effect is less pronounced for orientation #2, probably because of a reduced number of interactions of gliding dislocations with interfaces in single slip mode compared to multiple slip mode (orientation #1).

The clustering effect characterized experimentally in 3.4 is not as marked in simulated maps of Fig. 12. For orientation #2, some high GND densities are found in regions of clustered particles with low particle interspacing. However, it is less clear for orientation #1. This can be attributed to the difference in grain size and orientation between EBSD maps and performed simulations. It suggests that the GND affected zone near particles can be modified by these two parameters.

Discussion

Our EBSD-based investigation of GND densities in a deformed Fe-TiB_2 composite shows that among the microstructural features acting as barriers to dislocation motion, matrix/particle interfaces play a major role. As seen on the EBSD map of Fig. 6, GND pile-ups form at matrix/particle interfaces and extend in the surrounding matrix with increasing deformation. This gives an experimental evidence of the predominance of plastic incompatibility between matrix and reinforcements in metal-matrix composites [46, 50, 51].

To our best knowledge, it is the first time that such an effect is quantified in the early stages of plastic deformation. Studies dealing with experimental characterization of deformation in MMCs at the microstructure scale are rather rare in the literature. In situ digital image correlation (DIC) tensile tests performed on cold-rolled Fe-TiB_2 microstructure evidence difficulties for accurate strain measurements at matrix/particles interfaces [11]. As for EBSD analysis, the main challenge relies on the surface preparation. It has to be optimized in order to accurately probe orientations close to the interface between the soft matrix and the hard particles. Therefore, most of the experimental research focuses on the overall macroscopic behavior and on the identification and quantification of damage processes in particulate-reinforced composites.

Our result has also highlighted that the plastic deformation is very heterogeneous along the interfaces. Hot spots of GND densities are located at the tips of elongated particles, acting as regions of important plastic strain incompatibility. This result conforms to recent observations for a similar TiB_2-reinforced steel [10] in which highly localized plastic flow investigated by means of DIC was found at the poles of large particles, while plastic strain seemed inhibited at their sides. This shape effect was also observed earlier for Al matrix composites [52].

This study also demonstrates the predominant effect of particle interspacing on plastic strain localization. No matter the macroscopic strain level, higher GND densities were observed in regions where the distance between neighboring particles is low (Fig. 10a), i.e., particle clusters. This result is consistent with previous finite element-based predictions for other MMCs (see reviews [50, 51]), which are here confirmed via experimental characterization of plastic deformation at the mesoscopic scale. The predominance of particle interspacing effect inferred from Fig. 10a could be even stronger as the statistical representation is biased by the position of particles inside the microstructure. Indeed, considering all EBSD scans, it can be evaluated that 70.2% of particles have more than two ferrite grain neighbors—i.e., are positioned at ferrite grain boundaries or triple points—while the remaining 29.8% are embedded within ferrite grains. Therefore, part of measured GND densities that were counted as close to grain boundaries or triple points in Fig. 10b, d ($d_{GB} < 1$ μm) also belong to the vicinity of a particle ($d_{CP} < 1$ μm). As no correlation between particle aspect ratio or sizes and local GND densities can be inferred from Fig. 6, it is expected that the spatial distribution of particles (especially in the form of clusters) has a stronger influence on plastic deformation mechanisms than the morphological parameters of individual particles.

Finally, the comparison of GND maps and associated BSE images at high voltage indicates that the EBSD data are subjected to a "3D effect" of particles present under the scanned surface (see Fig. 8). Indeed, locally high GND densities detected in the center of ferrite grains are quite systematically the consequence of particles present deeper in the volume of the matrix. This confirms that plastic deformation measured at the surface of a composite is affected by subsurface microstructural features.

Similar assumptions were made in [11] considering the surface strain fields derived from DIC tests of a hot-rolled Fe-TiB_2 steel. This suggests performing additional 3D analysis using a dual-beam microscope equipped with EBSD [53, 54]. Such set of data would give the complete three-dimensional morphology of particles and improve local correlations between GND density close to TiB_2 particles and their morphological features (as size and aspect ratio).

Numerical results described in Sect. 4 have shown that the MFDM-EVP-FFT model builds upon conventional crystal plasticity (CP) models to capture dislocation pile-ups at the particle/matrix interfaces. Indeed, in classic CP models, strain hardening only depends on crystallographic slip variables, whereas in the non-local MFDM formulation, the introduction of Nye's dislocation density tensor allows accounting for dislocations explicitly, and effects of GNDs on hardening are not ignored. This renders the macroscopic response and mesoscopic fields dependent on internal lengths of the microstructure [31]. Similarly, in [19], intra-granular slip gradients were predicted in channels of two-phase laminates using MFDM-EVP-FFT resulting in a continuous double-ended GND pile-up at interfaces, unlike uniform slip in the channel was obtained with CP-EVP-FFT resulting in just a dipole of GNDs located at the phase boundaries. These MFDM predictions are also similar to the case of grain size effects in polycrystals, which were correctly described and related to the increase and spreading of intra-granular GND densities [20, 55].

In this study, the increase in the GND layer close to TiB_2 particles is of importance to understand the mechanical behavior of the investigated composite. Indeed, as a result of this GND density accumulation, the effective particle interspacing available for free dislocation motion is reduced with further load [56] and long-range internal stress gradients develop inside the ferrite grains, as was also reported in earlier work in synthetic microstructures representing Fe-TiB_2 [31]. These internal stress gradients are at the origin of "back-stresses" opposed to the external load, which cause further hardening on the macroscopic behavior of the composite and may influence reversible plasticity. In [20], cyclic plasticity was investigated in polycrystalline volumes using MFDM-EVP-FFT and strong Bauschinger effects were predicted without the introduction of any phenomenological kinematic hardening or ad-hoc back-stress variable in the constitutive model. Both kinematic and isotropic hardening contributions were found to be higher than conventional CP results. This is due to these predicted long-range internal stress gradients, which is different from the classic composite effect in CP.

In this study, a log-normal probability density function of GND densities was obtained using MFDM-EVP-FFT with average and standard deviation increasing with tensile strains (see Fig. 11) as a result of GND accumulation at interfaces. This trend is in agreement with the experimental distributions of GND densities for specimens deformed with increasing strain (see Fig. 4). The spatial localization of dislocation structures was shown to conform to the spatial distribution of particles and their morphology. The MFDM-EVP-FFT model can then be used as a complementary tool to investigate the effect of specific topologies and distributions of particles on the deformation substructures and the materials ductility later during plastic deformation.

Conclusions

This study has experimentally examined and numerically predicted the development of deformation heterogeneities through the accumulation of GND densities in a Fe-TiB_2 composite plastically deformed under uniaxial tension. From the analysis of 2D EBSD orientation maps, the following conclusions can be drawn:

- The orientation precision of EBSD data was estimated at 0.12°. Obtaining this rather low value of precision in the soft matrix is quite challenging due to the strong stiffness contrast with TiB_2 particles. However, it is a prerequisite for the study of deformation mechanisms at low strains. It was here enabled by the use of high-resolution EBSD patterns analyzed in "refined accuracy" mode and an optimized surface preparation.

- A heterogeneous distribution of GND densities develops with increasing plastic strain: Fe/TiB_2 interfaces are regions of high plastic strain incompatibilities where GND pile-ups and walls are formed and spread within the surrounding matrix. Correlations between evaluated GND densities in the matrix and distances to the nearest particles showed that the particle interspacing is a key feature for strain localization. Its contribution is predominant over the contribution of grain

boundaries (i.e., grain size and triple point effects), at least up to 6% of strain.

- The localization of the deformation is also affected by the particle morphology. GND density maps derived from EBSD data showed that larger and more intense GND pile-ups are formed at the tips of elongated particles.
- In addition, full-field numerical simulations were performed using the MFDM-EVP-FFT theory. These simulations informed by experimental particle distribution derived from 2D EBSD maps showed satisfactory qualitative agreement with the GND statistical distributions derived from experimental data. In contrast with conventional crystal plasticity models, the MFDM-EVP-FFT model was also able to qualitatively reproduce the progressive accumulation of GNDs close to TiB_2 particles, including the effect of particle morphological features. The results of such simulations are useful in the context of industrial R&D to inform the design of optimized Fe-TiB_2 microstructures.

Acknowledgements

This study was conducted in the frame of a Carnot ARTS project in collaboration with J.-P. Chevalier and co-workers at PIMM Laboratory (CNAM, Arts et Métiers Paris Tech, CNRS). The authors thank the French State (ANR) through the program "Investment in Future" (LabEx "DAMAS" referenced as ANR-11-LABX-0008-01), ArcelorMittal Research Development and the Grand Est region for financial support. RAL acknowledges support from Los Alamos National Laboratory's Laboratory-Directed Research and Development (LDRD) program.

Data availability

The raw/processed data required to reproduce these findings cannot be shared at this time as the data also forms part of an ongoing study.

Declarations

Conflict of interest All authors declare that there is no conflict of interest with regard to the submission of this manuscript.

References

[1] Bouaziz O, Zurob H, Huang M (2010) Driving force and logic of development of advanced high strength steels for automotive applications. Steel Res Int 84(10):937–947

[2] Bonnet F, Daeschler V, Petitgand G (2014) High modulus steels: new requirement of automotive market How to take up challenge? Can Metall Q 53(3):243–252

[3] Munro RG (2000) Material properties of titanium diboride. J Res Nat Inst Stand Technol 105(5):709–720

[4] ARCELOR Research group, Patent EP 1 897 963 A1, Bulletin 2008/11, 20p.

[5] Rana R, Liu C (2014) Effects of ceramic particles and composition on elastic modulus of low density steels for automotive applications. Can Metall Q 53(3):300–316

[6] Aparicio-Fernández R, Springer H, Szczepaniak A, Zhang H, Raabe D (2016) In-situ metal matrix composite steels: effect of alloying and annealing on morphology, structure and mechanical properties of TiB2 particle containing high modulus steels. Acta Mater 107:38–48

[7] Wang X, Leng H, Han B, Wang X, Hu B, Luo H (2019) Solidified microstructures and elastic modulus of hypo-eutectic and hyper-eutectic TiB2-reinforced high-modulus steel. Acta Mater 176:84–95

[8] Dammak M, Gaspérini M, Barbier D (2014) Microstructural evolution of iron based metal–matrix composites submitted to simple shear. Mater Sci Eng, A 616:123–131

[9] Hadjem-Hamouche Z, Chevalier JP, Cui Y, Bonnet F (2012) Deformation behavior and damage evaluation in a new titanium diboride (TiB2) steel-based composite. Steel Res Int 83(6):538–545

[10] Li YZ, Luo ZC, Yi HL, Huang MX (2016) Damage mechanisms of a TiB2-reinforced steel matrix composite for lightweight automotive application. Metall Mater Trans E 3(3):203–208

[11] Hadjem-Hamouche Z, Derrien K, Héripré E, Chevalier JP (2018) In-situ experimental and numerical studies of the damage evolution and fracture in a Fe-TiB2 composite. Mater Sci Eng, A 724:594–605

[12] Chen R, Li B, Li Y, Liu Z, Long X, Yi H, Huang M (2020) Revealing the fatigue crack initiation mechanism of a TiB2-reinforced steel matrix composite. Int J Fatigue 130:105276

[13] Huang MX, He BB, Wang X, Yi HL (2015) Interfacial plasticity of a TiB2-reinforced steel matrix composite fabricated by eutectic solidification. Scripta Mater 99:13–16

[14] Li YZ, Huang MX (2018) Revealing the interfacial plasticity and shear strength of a TiB2-strengthened high-modulus low-density steel. J Mech Phys Solids 121:313–327

[15] Gee M, Mingard K, Roebuck B (2009) Application of EBSD to the evaluation of plastic deformation in the mechanical

testing of WC/Co hardmetal. Int J Refract Metal Hard Mater 27(2):300–312

[16] Guo J, Amira S, Gougeon P, Chen XG (2011) Effect of the surface preparation techniques on the EBSD analysis of a friction stir welded AA1100-B4C metal matrix composite. Mater Charact 62(9):865–877

[17] Smirnov AS, Belozerov GA, Smirnova EO, Konovalov AV, Shveikin VP, Muizemnek OY (2016) Specimen preparation for metal matrix composites with a high volume fraction of reinforcing particles for EBSD analysis. J Mater Eng Perform 25(7):2907–2913

[18] Lebensohn RA, Kanjarla AK, Eisenlohr P (2012) An elasto-viscoplastic formulation based on fast fourier transforms for the prediction of micromechanical fields in polycrystalline materials. Int J Plast 32:59–69

[19] Djaka KS, Berbenni S, Taupin V, Lebensohn RA (2020) A FFT-based numerical implementation of mesoscale field dislocation mechanics: application to two-phase laminates. Int J Solids Struct 184:136–152

[20] Berbenni S, Taupin V, Lebensohn RA (2020) A fast Fourier transform-based mesoscale field dislocation mechanics study of grain size effects and reversible plasticity in polycrystals. J Mech Phys Solids 135:103808

[21] Acharya A, Roy A (2006) Size effects and idealized dislocation microstructure at small scales: predictions of a phenomenological model of mesoscopic field dislocation mechanics: part I. J Mech Phys Solids 54(8):1687–1710

[22] Roy A, Puri S, Acharya A (2006) Phenomenological mesoscopic field dislocation mechanics, lower-order gradient plasticity, and transport of mean excess dislocation density. Modell Simul Mater Sci Eng 15(1):S167–S180

[23] Puri S, Das A, Acharya A (2011) Mechanical response of multicrystalline thin films in mesoscale field dislocation mechanics. J Mech Phys Solids 59(11):2400–2417

[24] Thomsen K, Schmidt NH, Bewick A, Larsen K, Goulden J (2013) Improving the accuracy of orientation measurements using EBSD. Microsc Microanal 19(S2):724–725

[25] B. Beausir J-J Fundenberger (2017) Analysis tools for electron and X-ray diffraction, ATEX - software, www.atex-software.eu, Université de Lorraine - Metz

[26] Pantleon W (2008) Resolving the geometrically necessary dislocation content by conventional electron backscattering diffraction. Scripta Mater 58(11):994–997

[27] Acharya A (2001) A model of crystal plasticity based on the theory of continuously distributed dislocations. J Mech Phys Solids 49(4):761–784

[28] Acharya A (2003) Driving forces and boundary conditions in continuum dislocation mechanics proceedings of the royal society of London series a: mathematical. Phys Eng Sci 459(2034):1343–1363

[29] Acharya A (2004) Constitutive analysis of finite deformation field dislocation mechanics. J Mech Phys Solids 52(2):301–316

[30] Acharya A, Roy A, Sawant A (2006) Continuum theory and methods for coarse-grained, mesoscopic plasticity. Scripta Mater 54(5):705–710

[31] Genée J, Berbenni S, Gey N, Lebensohn RA, Bonnet F (2020) Particle interspacing effects on the mechanical behavior of a Fe–TiB 2 metal matrix composite using FFT-based mesoscopic field dislocation mechanics. Adv Model Simul Eng Sci 7(1):1–23

[32] Moulinec H, Suquet P (1994) A fast numerical method for computing the linear and non linear properties of composites. CR de l'Académie des Sci Paris II 318:1417–1423

[33] Moulinec H, Suquet P (1998) A numerical method for computing the overall response of nonlinear composites with complex microstructure. Comput Methods Appl Mech Eng 157:69–94

[34] Okamoto NL, Kusakari M, Tanaka K, Inui H, Otani S (2010) Anisotropic elastic constants and thermal expansivities in monocrystal CrB2, TiB2, and ZrB2. Acta Mater 58(1):76–84

[35] Nolze G, Jürgens M, Olbricht J, Winkelmann A (2018) Improving the precision of orientation measurements from technical materials via EBSD pattern matching. Acta Mater 159:408–415

[36] Nicolaÿ A, Franchet JM, Cormier J, Mansour H, De Graef M, Seret A, Bozzolo N (2019) Discrimination of dynamically and post-dynamically recrystallized grains based on EBSD data: application to Inconel 718. J Microsc 273(2):135–147

[37] Nolze G, Hielscher R, Winkelmann A (2017) Electron backscatter diffraction beyond the mainstream. Cryst Res Technol 52(1):1600252

[38] Saada MB, Gey N, Beausir B, Iltis X, Mansour H, Maloufi N (2017) Sub-boundaries induced by dislocational creep in uranium dioxide analyzed by advanced diffraction and channeling electron microscopy. Mater Charact 133:112–121

[39] Winkelmann A, Jablon BM, Tong VS, Trager-Cowan C, Mingard KP (2020) Improving EBSD precision by orientation refinement with full pattern matching. J Microsc 277(2):79–92

[40] Wilkinson AJ, Meaden G, Dingley DJ (2006) High resolution mapping of strains and rotations using electron backscatter diffraction. Mater Sci Technol 22(11):1271–1278

[41] C. Ernould, B. Beausir, J.J. Fundenberger, V. Taupin, E. Bouzy (2020) Global DIC approach guided by a cross-correlation based initial guess for HR-EBSD and on-axis HR-TKD. Acta Mater 191:131–148

[42] Muransky O, Balogh L, Tran M, Hamelin CJ, Park JS, Daymond MR (2019) On the measurement of dislocations

and dislocation substructures using EBSD and HRSD techniques. Acta Mater 175:297–313

[43] Wilkinson AJ, Randman D (2010) Determination of elastic strain fields and geometrically necessary dislocation distributions near nanoindents using electron back scatter diffraction. Phil Mag 90(9):1159–1177

[44] Allain-Bonasso N, Wagner F, Berbenni S, Field DP (2012) A study of the heterogeneity of plastic deformation in IF steel by EBSD. Mater Sci Eng, A 548:56–63

[45] Ashby MF (1970) The deformation of plastically non-homogeneous materials,. Philos Mag J Theor Exp Appl Phys 21(170):399–424

[46] Gustafson TW, Panda PC, Song G, Raj R (1997) Influence of microstructural scale on plastic flow behavior of metal matrix composites. Acta Mater 45(4):1633–1643

[47] Jiang J, Britton TB, Wilkinson AJ (2013) Evolution of dislocation density distributions in copper during tensile deformation. Acta Mater 61(19):7227–7239

[48] Zhu C, Harrington T, Gray GT III, Vecchio KS (2018) Dislocation-type evolution in quasi-statically compressed polycrystalline nickel. Acta Mater 155:104–116

[49] SI Wright DP Field MM Nowell (2015) Post processing effects on GND calculations from EBSD-based orientation measurements, In: *IOP Conference Series*: *Materials Science and Engineering* 89(1):012049, IOP Publishing

[50] Mortensen A, Llorca J (2010) Metal matrix composites. Annu Rev Mater Res 40:243–270

[51] Chawla N, Shen YL (2001) Mechanical behavior of particle reinforced metal matrix composites. Adv Eng Mater 3(6):357–370

[52] Soppa E, Schmauder S, Fischer G, Thesing J, Ritter R (1999) Influence of the microstructure on the deformation behaviour of metal–matrix composites. Comput Mater Sci 16(1–4):323–332

[53] Guyon J, Gey N, Goran D, Chalal S, Perez-Willard F (2016) Advancing FIB assisted 3D EBSD using a static sample setup. Ultramicroscopy 161:161–167

[54] Konijnenberg PJ, Zaefferer S, Raabe D (2015) Assessment of geometrically necessary dislocation levels derived by 3D EBSD. Acta Mater 99:402–414

[55] Cordero NM, Forest S, Busso EP, Berbenni S, Cherkaoui M (2012) Grain size effects on plastic strain and dislocation density tensor fields in metal polycrystals. Comput Mater Sci 52(1):7–13

[56] Groh S, Devincre B, Kubin LP, Roos A, Feyel F, Chaboche JL (2005) Size effects in metal matrix composites. Mater Sci Eng A 400:279–282